Square skyrmion lattice in multi-orbital f-electron systems

Yan Zha ◉[1, *] and Satoru Hayami ◉[1, †]

[1] *Graduate School of Science, Hokkaido University, Sapporo 060-0810, Japan*
(Dated: May 1, 2025)

[a] We report the emergence of a square-shaped skyrmion lattice in multi-orbital f-electron systems with easy-axis magnetic anisotropy on a centrosymmetric square lattice. By performing mean-field calculations for an effective localized model consisting of two Kramers doublets, we construct the low-temperature phase diagram in a static external magnetic field. Consequently, we find that a square-shaped skyrmion lattice with the skyrmion number of one appears in the intermediate-field region when the crystal field splitting between the two doublets is small. Furthermore, we identify another double-Q state with a nonzero net scalar chirality at zero- and low-field regions, which is attributed to the help of the multi-orbital degree of freedom. Our results offer another route to search for skyrmion-hosting materials in centrosymmetric f-electron tetragonal systems with multi-orbital degrees of freedom, e.g., Ce-based compounds. This contrasts with conventional other f-electron systems hosting skyrmion lattices, such as Gd- and Eu-based compounds without orbital angular momentum.

I. INTRODUCTION

Skyrmions, a class of quasi-particles, were first proposed by Tony Skyrme in the 1960s [1], describing a type of topologically stable field configuration. Subsequently, they have become a significant topic in condensed matter physics [2–8]. Due to their topological nature, skyrmions remain invariant under continuous deformations [5], which has led to active research into their stability [9–12]. Their topological robustness and unconventional transport properties have garnered increasing attention in spintronics, and skyrmions hold great promise for applications, making them strong candidates for next-generation computing and storage devices [6, 13–15].

Compared to a single skyrmion, a skyrmion lattice (SkL) is a highly ordered structure as a thermodynamic phase. The conventional microscopic mechanism for the formation of SkLs is the synergy of the ferromagnetic exchange interaction, the Dzyaloshinskii–Moriya (DM) interaction [16, 17], and the Zeeman coupling induced by a static external magnetic field in noncentrosymmetric magnets [2–4, 18]. This naturally prompts the question of whether SkLs can arise in a system without spatial inversion symmetry breaking. Experimental advances in recent years have shown that centrosymmetric materials with spatial inversion symmetry can indeed host SkLs under an external magnetic field. Examples include Gd_2PdSi_3 [19–23] on a triangular-lattice hexagonal structure and $Gd_3Ru_4Al_{12}$ [24–26] on a kagome-type hexagonal structure and $GdRu_2Si_2$ [27–29], $EuAl_4$ [30–34], and $GdRu_2Ge_2$ [35] on a centrosymmetric tetragonal lattice. Although the DM interaction leading to the SkLs does not exist in systems with inversion symmetry, several microscopic mechanisms have been theoretically proposed to stabilize the SkLs [36], such as competing exchange interactions [37–39], dipolar interactions [40, 41], nonmagnetic impurity [42], crystal-dependent magnetic anisotropy [43–46], and electric-field-induced three-spin interactions [47].

Specifically, we focus on the square-shaped SkL (S-SkL), where skyrmions are packed so as to satisfy the fourfold rotational symmetry on a two-dimensional square lattice. The S-SkL is described by a double-Q state, which is formed by a superposition of two spiral waves with mutually perpendicular wave vectors. From an energetic viewpoint, the formation of such a double-Q S-SkL is severe compared to that of a triple-Q triangular-shaped SkL with the ordering wave vectors Q_1, Q_2, and Q_3, the latter of which has an effective fourth-order coupling in the free energy owing to the relation of $Q_1 + Q_2 + Q_3 = 0$ [39, 48]. Indeed, it has been revealed that the S-SkL in centrosymmetric systems appears in the ground state by considering additional effects, such as biquadratic interaction [49], compass-type anisotropic interaction [40, 50], higher-harmonic wave vector interaction [51], and long-range magnetic anisotropy [52]. These theoretical studies offer microscopic mechanisms of the S-SkLs observed in experimental materials, as mentioned above, as well as candidate materials hosting the S-SkL, such as $EuGa_4$ [53, 54], $EuGa_2Al_2$ [55], $Mn_{2-x}Zn_xSb$ [56], and $GdOs_2Si_2$ [57].

Meanwhile, one notices that, to date, most materials hosting the S-SkLs contain $4f$ lanthanoid elements without the orbital angular momentum like Gd and Eu ions. This fact motivates us to explore whether the S-SkLs are possible in other $4f$-electron compounds with the orbital angular momentum, such as Ce ions. Moreover, most previous studies

have been performed for the effective spin models by renormalizing or ignoring the orbital degree of freedom. In other words, the multi-orbital effect on the S-SkLs has not been fully elucidated.

In the present study, we theoretically incorporate the multi-orbital effect in order to further understand the stabilization mechanism of the S-SkL in centrosymmetric hosts. We specifically consider the localized model consisting of two Kramers doublets with the f^1 configuration under strong easy-axis magnetic anisotropy as a consequence of the interplay between the spin–orbit interaction and crystalline electric field on the square lattice. Within the mean-field calculations for the localized model, we show that several double-Q states including the S-SkL and another double-Q state with a net scalar chirality emerge in the low-temperature phase diagram depending on the external magnetic field and crystalline electric field: The former is the fourfold-symmetric S-SkL with the skyrmion number of one, which is stabilized in the intermediate-field region and the latter is the fourfold-asymmetric double-Q state with inequivalent intensities at two ordering wave vectors, which is stabilized from zero- to low-field region. We identify these topologically nontrivial states by examining the structure factor, local and net scalar chirality, magnetization, and topological skyrmion number. Our results can be applicable to $4f$-electron compounds with the f^1 configuration like the Ce-based compounds.

The rest of the paper is organized as follows. In Sec. II, we introduce an effective localized model that includes the exchange interaction, the Zeeman coupling, and the crystal field splitting between the two Kramers doublets under the spin–orbit coupling and tetragonal crystalline electric field. In Sec. III, we present the numerical mean-field method used to investigate the ground state under different external magnetic fields and crystal field splittings, and we provide multiple physical quantities to collectively characterize the S-SkL and the other multi-Q magnetic-moment configurations. In Sec. IV, we report the low-temperature phase diagram for the localized model, elucidate the mechanism behind the formation of the S-SkL, and discuss in detail the other magnetic phases. Finally, in Sec. V, we summarize the results of the present paper. In Appendix A, we show the derivation of the low-energy atomic bases in the effective localized model. In Appendix B, we examine the stability of the S-SkL phase when one of the crystal field parameters α is varied.

II. MODEL

We consider the situation where the $4f$ electrons are well localized at each lattice site on the two-dimensional square lattice. In addition, we suppose the f^1 configuration with the Ce^{3+} ion in mind. When both effects of the atomic spin–orbit coupling and the tetragonal crystalline electric field are taken into account, the fourteen-degenerated energy levels with the total orbital angular momenta $J = 7/2$ and $J = 5/2$ are split into seven Kramers doublets, as detailed in Appendix A. We construct an effective localized model by choosing two out of seven Kramers doublets, whose atomic bases are represented by using the notation $|J, J_z\rangle$ as

$$\begin{cases} \left|\Gamma_{t7\pm}^{(1)}\right\rangle = \alpha \left|\tfrac{5}{2}, \pm\tfrac{5}{2}\right\rangle - \beta \left|\tfrac{5}{2}, \mp\tfrac{3}{2}\right\rangle, \\ \left|\Gamma_{t7\pm}^{(2)}\right\rangle = \beta \left|\tfrac{5}{2}, \pm\tfrac{5}{2}\right\rangle + \alpha \left|\tfrac{5}{2}, \mp\tfrac{3}{2}\right\rangle, \end{cases} \tag{1}$$

where

$$\alpha = \frac{2\sqrt{5}\, B_4^4}{\sqrt{\left(\sqrt{X^2 + 20\left(B_4^4\right)^2} + X\right)^2 + 20\left(B_4^4\right)^2}}, \tag{2}$$

$$X = \left(B_2^0 + 20\, B_4^0\right), \tag{3}$$

$$\beta^2 = 1 - \alpha^2, \tag{4}$$

with the crystal field parameters B_2^0, B_4^0, and B_4^4 under the tetragonal symmetry (see Appendix A in detail). Then, the effective localized Hamiltonian is given by

$$\mathcal{H}_{\text{tot}} = \mathcal{H}_{\text{ex}} + \mathcal{H}_\Delta + \mathcal{H}_Z, \tag{5}$$

$$\mathcal{H}_{\text{ex}} = -\sum_{\langle i,j\rangle} \mathcal{J}_{ij} \boldsymbol{J}_i \cdot \boldsymbol{J}_j, \tag{6}$$

$$\mathcal{H}_\Delta = \begin{pmatrix} 0 & 0 & 0 & 0 \\ 0 & 0 & 0 & 0 \\ 0 & 0 & \Delta & 0 \\ 0 & 0 & 0 & \Delta \end{pmatrix}, \tag{7}$$

$$\mathcal{H}_Z = -h\sum_i J_i^z, \tag{8}$$

where the total Hamiltonian $\mathcal{H}_{\text{tot}}$ includes the contributions from the exchange interactions in $\mathcal{H}_{\text{ex}}$, crystal field splitting in $\mathcal{H}_\Delta$, and the Zeeman coupling in $\mathcal{H}_Z$. We suppose that the ground-state energy level is $\left|\Gamma_{t7\pm}^{(1)}\right\rangle$ and the first-excited energy level is $\left|\Gamma_{t7\pm}^{(2)}\right\rangle$, as often found in Ce-based compounds, such as CeRhIn$_5$ and CeCoIn$_5$ [58]. Here, $\boldsymbol{J}_i$ represents the localized total angular momentum operator $\boldsymbol{J}_i$ at site i, whose matrix elements for the bases $\left\{\left|\Gamma_{t7+}^{(1)}\right\rangle, \left|\Gamma_{t7-}^{(1)}\right\rangle, \left|\Gamma_{t7+}^{(2)}\right\rangle, \left|\Gamma_{t7-}^{(2)}\right\rangle\right\}$ are expressed as

$$J^x = \begin{pmatrix} 0 & -\sqrt{5}\alpha\beta & 0 & \frac{1}{2}\sqrt{5}(\alpha-\beta)(\alpha+\beta) \\ -\sqrt{5}\alpha\beta & 0 & \frac{1}{2}\sqrt{5}(\alpha-\beta)(\alpha+\beta) & 0 \\ 0 & \frac{1}{2}\sqrt{5}(\alpha-\beta)(\alpha+\beta) & 0 & \sqrt{5}\alpha\beta \\ \frac{1}{2}\sqrt{5}(\alpha-\beta)(\alpha+\beta) & 0 & \sqrt{5}\alpha\beta & 0 \end{pmatrix}, \tag{9}$$

$$J^y = \begin{pmatrix} 0 & i\sqrt{5}\alpha\beta & 0 & -\frac{1}{2}i\sqrt{5}(\alpha-\beta)(\alpha+\beta) \\ -i\sqrt{5}\alpha\beta & 0 & \frac{1}{2}i\sqrt{5}(\alpha-\beta)(\alpha+\beta) & 0 \\ 0 & -\frac{1}{2}i\sqrt{5}(\alpha-\beta)(\alpha+\beta) & 0 & -i\sqrt{5}\alpha\beta \\ \frac{1}{2}i\sqrt{5}(\alpha-\beta)(\alpha+\beta) & 0 & i\sqrt{5}\alpha\beta & 0 \end{pmatrix}, \tag{10}$$

$$J^z = \begin{pmatrix} \frac{1}{2}\left(5\alpha^2 - 3\beta^2\right) & 0 & 4\alpha\beta & 0 \\ 0 & \frac{1}{2}\left(3\beta^2 - 5\alpha^2\right) & 0 & -4\alpha\beta \\ 4\alpha\beta & 0 & \frac{1}{2}\left(5\beta^2 - 3\alpha^2\right) & 0 \\ 0 & -4\alpha\beta & 0 & \frac{1}{2}\left(3\alpha^2 - 5\beta^2\right) \end{pmatrix}. \tag{11}$$

It is noted that $\boldsymbol{J}$ is anisotropic in this Hilbert space, which arises from the spin–orbit coupling and crystalline electric field.

For the above atomic bases, we consider the exchange interactions between different sites, as represented by $\mathcal{H}_{\text{ex}}$ [59]. In order to consider the finite-q magnetic instability, we consider the frustrated exchange interactions consisting of the first-, second-, and third-neighbor interactions on the square lattice, whose coupling constants are denoted as J_1, J_2, and J_3, respectively. We choose these exchange parameters so that the ordering wave vectors are located at finite-q positions in momentum space. This is demonstrated by the Fourier transformation of $\mathcal{H}_{\text{ex}}$ leading to

$$\mathcal{H}_{\text{ex}} = -\sum_{\boldsymbol{q}} \boldsymbol{J}_{\boldsymbol{q}} \cdot \boldsymbol{J}_{-\boldsymbol{q}} \, \mathcal{J}(\boldsymbol{q}), \tag{12}$$

where $\boldsymbol{q}$ represents the wave vector and

$$\boldsymbol{J}_i = \frac{1}{\sqrt{N}} \sum_{\boldsymbol{q}} \boldsymbol{J}_{\boldsymbol{q}} \exp\left(i\,\boldsymbol{q}\cdot\boldsymbol{r}_i\right). \tag{13}$$

Here, $\boldsymbol{r}_i$ is the position vector of site i. From the above expression, the relation $\boldsymbol{J}_{\boldsymbol{q}}^* = \boldsymbol{J}_{-\boldsymbol{q}}$ holds, which ensures that $\boldsymbol{J}_{\boldsymbol{q}} \cdot \boldsymbol{J}_{-\boldsymbol{q}}$ is a real number. The quantity $\mathcal{J}(\boldsymbol{q})$ is also real and defined as

$$\mathcal{J}(\boldsymbol{q}) = \sum_{\boldsymbol{r}_i - \boldsymbol{r}_j} \mathcal{J}_{ij}(\boldsymbol{r}_i - \boldsymbol{r}_j) \exp\left[i\,\boldsymbol{q}\cdot(\boldsymbol{r}_i - \boldsymbol{r}_j)\right]$$
$$= \mathcal{J}(-\boldsymbol{q}) = \mathcal{J}(\boldsymbol{q})^*. \tag{14}$$

For the square lattice with the interactions J_1–J_3, $\mathcal{J}(\boldsymbol{q})$ is explicitly expressed as

$$\mathcal{J}(\boldsymbol{q}) = 2J_1(c_x + c_y) + 4J_2c_xc_y + 2J_3(c_{2x} + c_{2y}), \tag{15}$$

where $c_\mu = \cos(a\,q_\mu)$ and $c_{2\mu} = \cos(2a\,q_\mu)$ for $\mu = x, y$; a denotes the lattice constant of the square lattice, and we set $a = 1$ for simplicity. When the second and third terms in Eq. (5) are absent, the ordering wave vectors of the ground-state magnetic states are determined by the maximum value of $\mathcal{J}(\boldsymbol{q})$. We choose the short-period ordering wave vectors as $\boldsymbol{Q}_1 = \left(\frac{2\pi}{6}, \frac{2\pi}{6}\right)$ so as to keep computational costs relatively low, where J_1 is the energy unit of the model; the ground state is characterized by a helical state with $\boldsymbol{Q}_1$ or $\boldsymbol{Q}_2 = \left(-\frac{2\pi}{6}, \frac{2\pi}{6}\right)$ when the interaction is isotropic [60]. Although there are several combinations of (J_1, J_2, J_3) to give the ordering wave vector at $\boldsymbol{Q}_1$, we choose $J_1 = 1$, $J_2 = -0.5$, and $J_3 = -0.25$ so that the energy contribution from the $\boldsymbol{Q}_1 + \boldsymbol{Q}_2$ becomes large, since such a contribution plays an important role in enhancing the instability toward the SkL compared to the helical state [51].

The effect of crystal field splitting between two Kramers doublets is expressed as $\mathcal{H}_\Delta$. Although the parameter Δ is related to the crystal field parameters, B_0^2, B_0^4, and B_4^4, we combine the effects of these crystal field parameters into a single parameter Δ for simplicity. The effect of the magnetic field is represented by the Zeeman coupling in $\mathcal{H}_Z$, where we renormalize the Landé g factor into h for simplicity.

In the following calculations, we set $\alpha = 0.38$, which leads to the easy-axis anisotropic interaction in $\mathcal{H}_{ex}$, since the easy-axis magnetic anisotropy tends to stabilize the SkL in centrosymmetric magnets [38, 51, 61]. Then, we construct the magnetic phase diagram by varying Δ and h.

III. METHOD

In this section, we present the numerical method based on the mean-field calculations in Sec. III A. Then, we present physical quantities to identify obtained magnetic phases in Sec. III B.

A. Mean-Field Calculations

In order to search for the instability toward the S-SkL in the effective localized model, we adopt the mean-field approximation to the exchange interaction Hamiltonian $\mathcal{H}_{ex}$, where the two-body interactions reduce to a single-body problem as follows [62]:

$$\mathcal{H}_{ex}^{MF} = -\sum_{\langle i,j \rangle} \mathcal{J}_{ij} \left(\boldsymbol{J}_i \cdot \langle \boldsymbol{J}_j \rangle + \boldsymbol{J}_j \cdot \langle \boldsymbol{J}_i \rangle - \langle \boldsymbol{J}_i \rangle \cdot \langle \boldsymbol{J}_j \rangle \right). \tag{16}$$

Then, one can directly diagonalize the total Hamiltonian and obtain the eigenvalues ϵ_n and eigenstates $|n\rangle$. The expectation values of the observables $\mathcal{O}$ at the temperature T is given by [63]

$$\langle \mathcal{O} \rangle = \frac{1}{Z} \sum_n \exp(-\epsilon_n/T) \langle n| \mathcal{O} |n\rangle, \tag{17}$$

where Z is the partition function,

$$Z = \sum_n \exp(-\epsilon_n/T), \tag{18}$$

where we set the Boltzmann constant k_B to unity. The unit of the temperature T is the exchange interaction J_1.

We iterate the mean-field calculations until both the free energy and mean values of magnetic moments at each lattice site converge to the precision of 10^{-6}. Since we consider the situation where the ordering wave vectors are $\boldsymbol{Q}_1$, we set a 6×6 unit cell under the periodic boundary conditions along both x and y directions. When the S-SkL characterized by the superposition of $\boldsymbol{Q}_1$ and $\boldsymbol{Q}_2$ is realized, two magnetic unit cells are included in the 6×6 unit cell.

In addition, we set the initial configurations of $\boldsymbol{J}_i$ as follows: We set up one ferromagnetic configuration, one single-Q spiral configuration, one double-Q spiral configuration, 10 conical configurations with different polar angles, and 200 SkL configurations that follow the formula in Ref. [40] in addition to approximately 200 random configurations. In the presence of the magnetic field $h > 0$, we additionally adopt 200 lowest-free-energy converged solutions from the previous calculation. Once the calculation for a given crystal field splitting Δ is completed, approximately 10 converged results around each h are also used as initial states for the subsequent calculation at each h. Furthermore, we introduce fluctuations in each converged magnetic moment at every site along x-, y−, and z-direction, ranging from -0.3 to 0.3, in the aforementioned 10 converged results around each h. These 10 fluctuated configurations are then used alongside the 10 original converged results for further calculations.

B. Physical Quantities

The obtained magnetic phases are identified by the structure factor and scalar chirality. The structure factor in terms of the magnetic moment $\boldsymbol{J}_i$ is given by

$$J(\boldsymbol{q}) = \frac{1}{N} \sum_{i,j} \langle \boldsymbol{J}_i \rangle \cdot \langle \boldsymbol{J}_j \rangle \exp\left[i\,\boldsymbol{q} \cdot (\boldsymbol{r}_i - \boldsymbol{r}_j)\right], \tag{19}$$

where $N = 36$ is the total number of sites.

In addition, we also calculate the scalar chirality in terms of the magnetic moments, which is defined by the triple scalar product as [18, 64]

$$\chi_i = \frac{1}{2} \sum_{\delta,\delta'=\pm 1} \delta\delta' \langle \boldsymbol{J}_i \rangle \cdot (\langle \boldsymbol{J}_{i+\delta\hat{x}} \rangle \times \langle \boldsymbol{J}_{i+\delta'\hat{y}} \rangle), \tag{20}$$

where $\hat{x}$ ($\hat{y}$) represents a translation by the lattice constant along the x (y) direction. Summing the local scalar chirality over all sites on the lattice gives the net scalar chirality $\langle \chi \rangle$, defined as

$$\langle \chi \rangle = \frac{1}{N} \sum_i \chi_i. \tag{21}$$

The vortex-like structure of a skyrmion is also characterized by the topological skyrmion number N_{sk}, which is defined via an integral of the solid angle [65, 66]. On a discrete lattice, this integral is replaced by a summation of local skyrmion densities, leading to the total skyrmion number as

$$N_{\mathrm{sk}} = \frac{1}{2} \frac{1}{4\pi} \sum_i \Omega_i. \tag{22}$$

A prefactor $\frac{1}{2}$ is due to the two magnetic unit cells in the 6×6 unit cell when the double-Q magnetic-moment configurations emerge. Here, $\Omega_i \in [-2\pi, 2\pi)$ is the skyrmion density [67], which is given by

$$\Omega_i = \sum_{\delta,\delta'=\pm 1} \arctan\left(\frac{2\delta\delta' \langle \boldsymbol{j}_i \rangle \cdot (\langle \boldsymbol{j}_j \rangle \times \langle \boldsymbol{j}_k \rangle)}{(\langle \boldsymbol{j}_i \rangle + \langle \boldsymbol{j}_j \rangle + \langle \boldsymbol{j}_k \rangle)^2 - 1}\right). \tag{23}$$

We normalize the magnetic moments as $\langle \boldsymbol{j}_i \rangle = \langle \boldsymbol{J}_i \rangle / |\langle \boldsymbol{J}_i \rangle|$; $j = i + \delta\hat{x}$ and $k = i + \delta'\hat{y}$. Since the topological skyrmion number N_{sk} counts how many times the magnetic-moment configuration wraps around the unit sphere, it becomes an integer. For example, $|N_{\mathrm{sk}}| = 1$ indicates a single skyrmion in the magnetic unit cell.

Furthermore, we calculate the net magnetization, which is defined as the vector sum of all mean magnetic moments divided by N:

$$\langle \boldsymbol{J} \rangle = \frac{1}{N} \sum_i \langle \boldsymbol{J}_i \rangle. \tag{24}$$

To quantitatively analyze the magnitude of the magnetization, we take the norm of $\langle \boldsymbol{J} \rangle$, denoted as $|\langle \boldsymbol{J} \rangle|$.

IV. RESULTS

Figure 1 shows the Δ–h phase diagram at low temperature $T = 0.05$, which is obtained by the mean-field calculations. The diagrams are constructed by varying h and Δ, and independently performing the iterations until the solutions converge for each initial magnetic-moment configuration.

We present eight types of real-space magnetic-moment configurations for each magnetic phase in Fig. 2(a). Although we perform the calculation in the 6×6 unit cell, we plot the 12×12 configurations by copying the original data for better visibility. To further enhance the readability of the image, the magnetic-moment lengths $|\langle \boldsymbol{J}_i \rangle|$ are normalized only when plotting the three-dimensional magnetic-moment configurations [68]. Additionally, we use the variation of the normalized polar angle θ' to depict the magnetic-moment orientation along the z-direction. The normalized polar

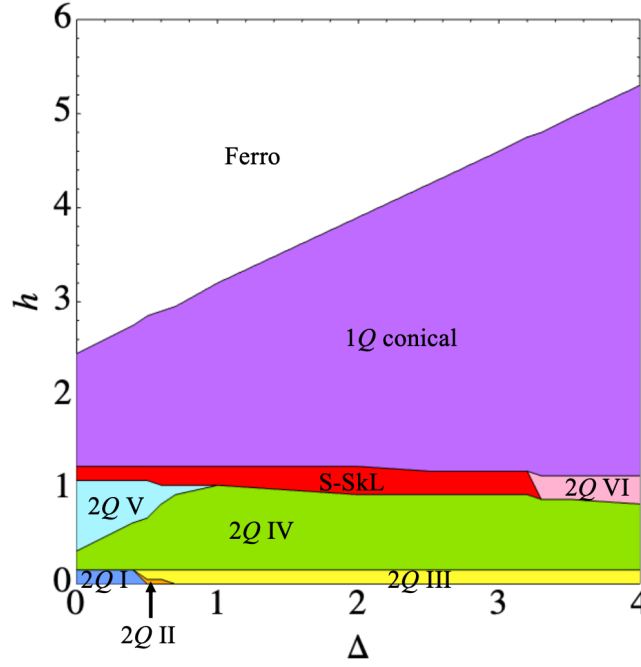FIG. 1. Phase diagram at low temperature ($T = 0.05$) as functions of the magnetic field h (vertical axis) and the crystal field splitting Δ between the two Kramers doublets (horizontal axis). Each colored region corresponds to a different low-temperature magnetic-moment configuration, including the $1Q$ conical magnetic phase, various $2Q$ phases (labeled I–VI), the S-SkL phase, and the ferromagnetic phase (Ferro).

angle θ' is defined as the ratio of the polar angle θ to π, with values ranging from 0 (north pole) to 1 (south pole) on the unit sphere.

Figure 2(b) displays the structure factor maps with respect to the magnetic moment in momentum space, with a rainbow color scheme representing the intensity of each structure factor. The axis labels n_x and n_y denote the multiples of $2\pi/6$, i.e., $n_x 2\pi/6$ and $n_y 2\pi/6$ for $-3 \leq n_x, n_y \leq 3$, in the first Brillouin zone. To further classify the magnetic-moment configurations, we decompose the structure factor into the in-plane one $J_{\boldsymbol{q}}^{xy} = J^x(\boldsymbol{q}) + J^y(\boldsymbol{q})$, and the out-of-plane one, $J_{\boldsymbol{q}}^z = J^z(\boldsymbol{q})$. These components are shown in Fig. 3, under three representative values of crystal field splitting i.e., $\Delta = 0, 0.5, 3.5$, with the top and middle panels corresponding to Fig. 3(a)–(c), respectively. Additionally, the bottom panels of Fig. 3(a)–(c) presents three graphs depicting the magnetization magnitude $|\langle \boldsymbol{J} \rangle|$, the absolute net scalar chirality $|\langle \chi \rangle|$, and the absolute skyrmion number $|N_{\rm sk}|$. We analyze data in the same manner as in Fig. 3 and list nonzero $J_{\boldsymbol{q}}^{xy}$ and $J_{\boldsymbol{q}}^z$ for the ordering wave vectors $\boldsymbol{Q}_1$ and $\boldsymbol{Q}_2$ as well as the higher-harmonic wave vectors $\boldsymbol{Q}'_1 = \boldsymbol{Q}_1 + \boldsymbol{Q}_2$ and $\boldsymbol{Q}'_2 = \boldsymbol{Q}_1 - \boldsymbol{Q}_2$ in each magnetic phase in Table I. In the double-Q configuration with $\boldsymbol{Q}_1$ and $\boldsymbol{Q}_2$, the contributions from high-harmonic wave vectors $\boldsymbol{Q}'_1$ and $\boldsymbol{Q}'_2$ become nonzero owing to the superposition of $\boldsymbol{Q}_1$ and $\boldsymbol{Q}_2$.

TABLE I. Nonzero components of $J_{\boldsymbol{Q}_\eta}$ and $J_{\boldsymbol{Q}'_\eta}$ ($\eta = 1, 2$) in each phase.

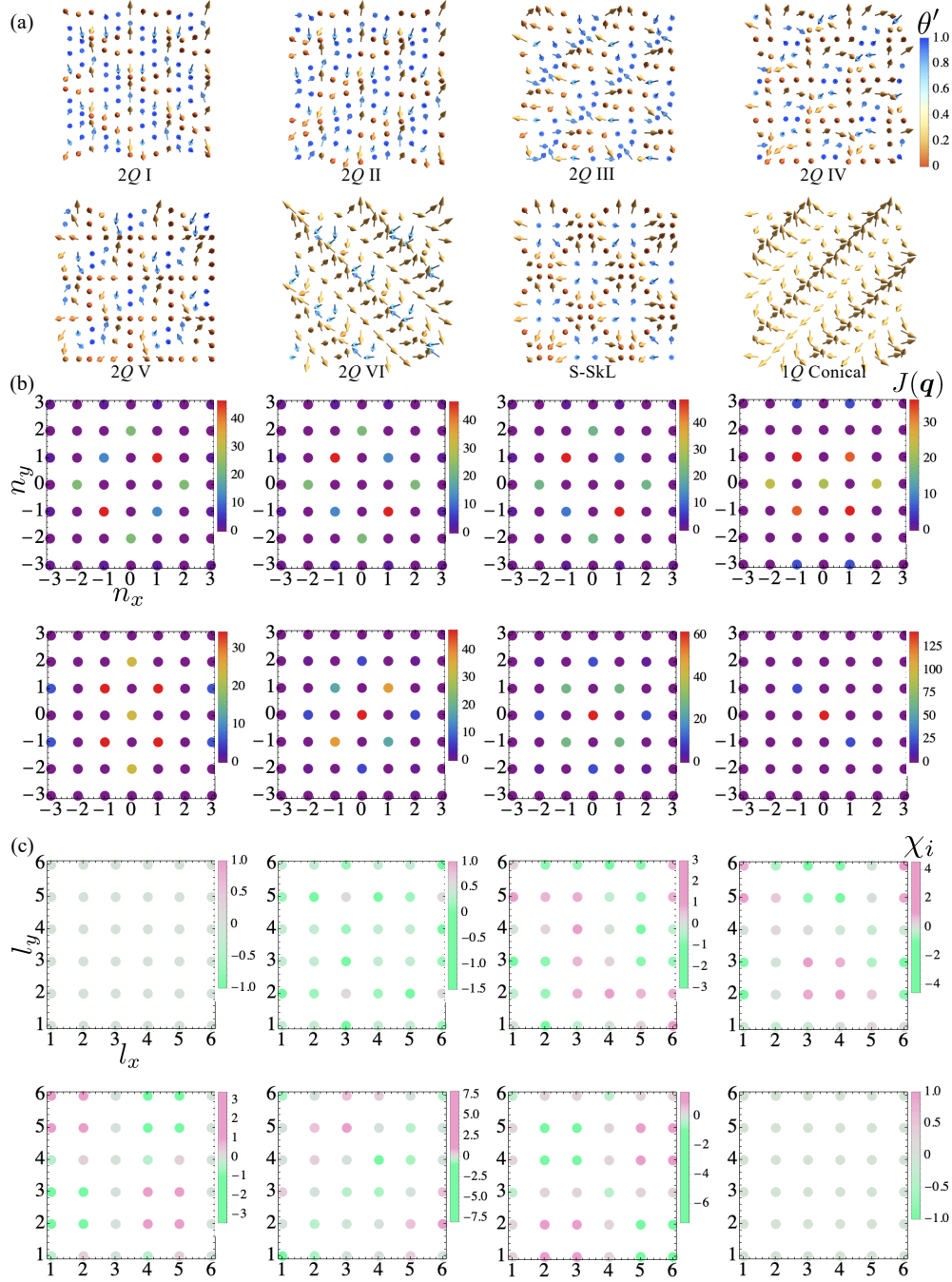| phase	$J_{\boldsymbol{Q}_1}, J_{\boldsymbol{Q}_2}$ ($\boldsymbol{Q}_\eta \parallel [110]$)	$J_{\boldsymbol{Q}'_1}, J_{\boldsymbol{Q}'_2}$ ($\boldsymbol{Q}'_\eta \parallel [100]$)
$1Q$ conical	$J_{\boldsymbol{Q}_1}^{xy}$	$-$
S-SkL	$J_{\boldsymbol{Q}_1}^{xy} = J_{\boldsymbol{Q}_2}^{xy}, J_{\boldsymbol{Q}_1}^z = J_{\boldsymbol{Q}_2}^z$	$J_{\boldsymbol{Q}'_1}^{xy} = J_{\boldsymbol{Q}'_2}^{xy}, J_{\boldsymbol{Q}'_1}^z = J_{\boldsymbol{Q}'_2}^z$
$2Q$ I	$J_{\boldsymbol{Q}_1}^{xy}, J_{\boldsymbol{Q}_2}^{xy}, J_{\boldsymbol{Q}_1}^z, J_{\boldsymbol{Q}_2}^z$	$J_{\boldsymbol{Q}'_1}^{xy} = J_{\boldsymbol{Q}'_2}^{xy}, J_{\boldsymbol{Q}'_1}^z = J_{\boldsymbol{Q}'_2}^z$
$2Q$ II	$J_{\boldsymbol{Q}_1}^{xy}, J_{\boldsymbol{Q}_2}^{xy}, J_{\boldsymbol{Q}_1}^z, J_{\boldsymbol{Q}_2}^z$	$J_{\boldsymbol{Q}'_1}^{xy} = J_{\boldsymbol{Q}'_2}^{xy}, J_{\boldsymbol{Q}'_1}^z = J_{\boldsymbol{Q}'_2}^z$
$2Q$ III	$J_{\boldsymbol{Q}_1}^{xy}, J_{\boldsymbol{Q}_2}^{xy}, J_{\boldsymbol{Q}_1}^z, J_{\boldsymbol{Q}_2}^z$	$J_{\boldsymbol{Q}'_1}^{xy} = J_{\boldsymbol{Q}'_2}^{xy}, J_{\boldsymbol{Q}'_1}^z, J_{\boldsymbol{Q}'_2}^z$
$2Q$ IV	$J_{\boldsymbol{Q}_1}^{xy}, J_{\boldsymbol{Q}_2}^{xy}, J_{\boldsymbol{Q}_1}^z = J_{\boldsymbol{Q}_2}^z$	$J_{\boldsymbol{Q}'_1}^z$
$2Q$ V	$J_{\boldsymbol{Q}_1}^{xy} = J_{\boldsymbol{Q}_2}^{xy}, J_{\boldsymbol{Q}_1}^z = J_{\boldsymbol{Q}_2}^z$	$J_{\boldsymbol{Q}'_1}^z$
$2Q$ VI	$J_{\boldsymbol{Q}_1}^{xy}, J_{\boldsymbol{Q}_1}^z = J_{\boldsymbol{Q}_2}^z$	$J_{\boldsymbol{Q}'_1}^z = J_{\boldsymbol{Q}'_2}^z$

FIG. 2. Panels (a)–(c) display three aspects of the real-space and momentum-space physical quantities: (a) Three-dimensional magnetic-moment configurations in a 6×6 unit cell, with magnetic moments drawn at each site and normalized in length for clarity. The color scale encodes the normalized polar angle $\theta' = \theta/\pi$, varying continuously from 0 (north pole) to 1 (south pole). (b) Structure factor distributions $J(\mathbf{q})$ regarding the magnetic moments in momentum space. The axis labels n_x and n_y denote the multiples of $2\pi/6$ with $-3 \leq n_x, n_y \leq 3$ in the first Brillouin zone. (c) Local scalar chirality χ_i in the 6×6 unit cell.

In Fig. 2(c), we show the local scalar chirality maps across all the lattice sites in the 6×6 unit cell, with a mint-colored scheme representing its intensity χ_i at each site. The axis labels l_x and l_y represent the lattice site indices with $1 \leq l_x, l_y \leq 6$. From the data of the structure factor in Fig. 2(b), Fig. 3, and Table I and the scalar chirality in
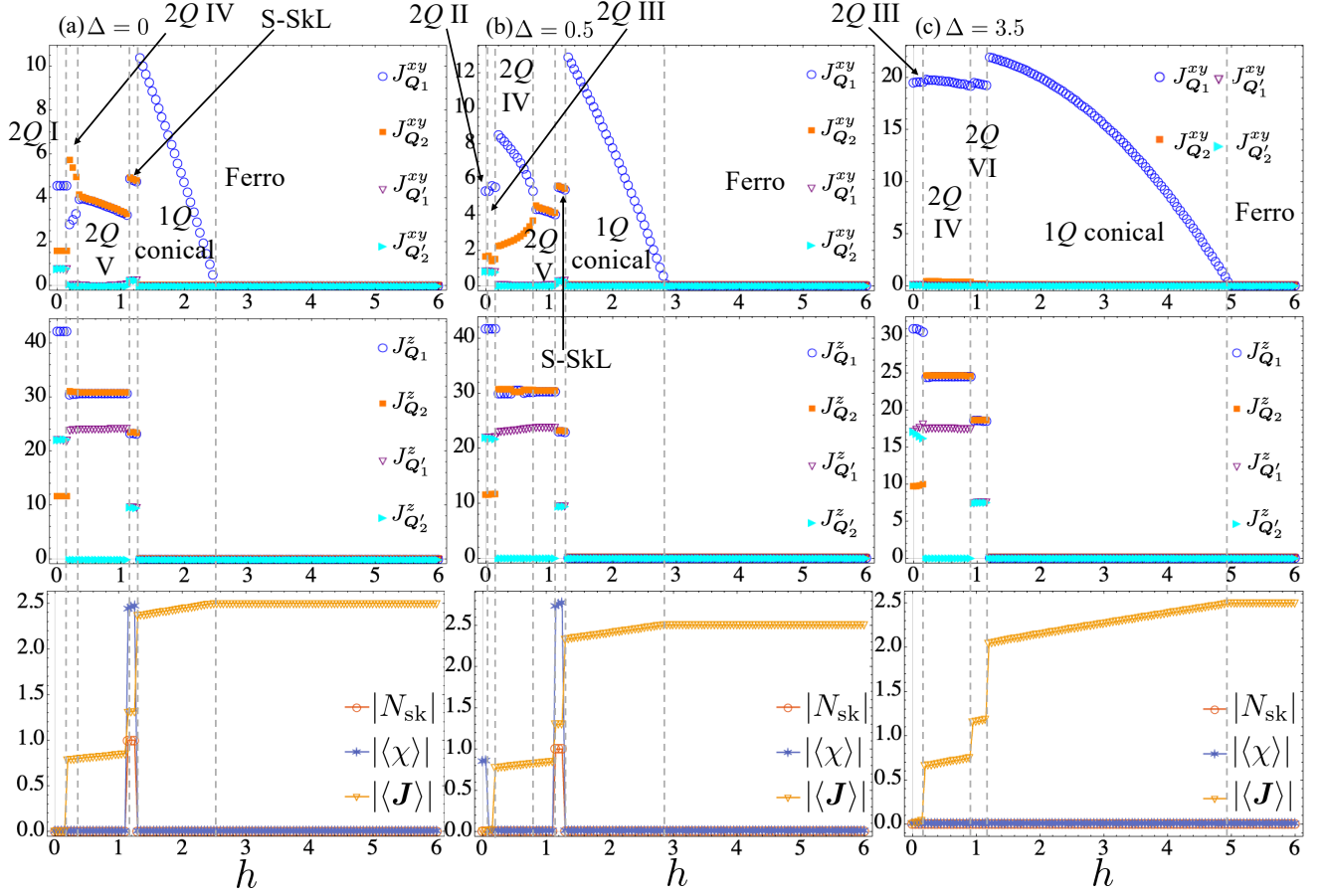
FIG. 3. Panels (a)–(c) display three representative values of crystal field splitting i.e., $\Delta = 0, 0.5, 3.5$, respectively. The top and middle panels of (a)–(c) illustrate the evolution of the in-plane structure factor component J_q^{xy} and the out-of-plane component J_q^z with respect to the external magnetic field h for the three representative crystal field splitting values. The bottom panels of (a)–(c) depict three physical quantities: the absolute topological skyrmion number $|N_{\rm sk}|$, the absolute scalar chirality $|\langle \chi \rangle|$, and the magnetization magnitude $|\langle \boldsymbol{J} \rangle|$. These graphs reveal the interplay between crystal field effects and external magnetic field on the magnetic-moment configurations.

Fig. 2(c) and Fig. 3, we distinguish magnetic phases in the phase diagram.

Among the obtained phases, the most important observation is the appearance of the S-SkL in the intermediate-field region of the phase diagram in Fig. 1. Specifically, this phase is stabilized when the crystal field splitting between the two doublets is approximately $0 \leq \Delta < 3.5$, and the magnetic field is around $h \simeq 1.1$. The region of the S-SkL becomes the largest when $\Delta \simeq 2$. This stability tendency indicates that the emergence of this S-SkL is owing to the multi-orbital effect that is often neglected by the classical spin model in previous studies. Indeed, the S-SkL disappears for large Δ, where the multi-orbital effect is negligible. Such a tendency is consistent with previous studies in the classical spin models; the S-SkL has been found only in the presence of the compass-type magnetic anisotropy [50] or dipolar interaction [40] or further neighbor interactions beyond the thrid-neighbor spins [52].

The behaviors of the magnetic moments in real and momentum spaces in the obtained S-SkL are similar to those in the classical spin models [51]. The S-SkL exhibits a net component of the scalar chirality, $\langle \chi \rangle \simeq 3$, which is influenced by the alterable magnetic-moment length and thus varies as Δ changes. The absolute value of the topological skyrmion number is $|N_{\rm sk}| = 1$, where the energy of the magnetic-moment configuration with $N_{\rm sk} = 1$ (antiskyrmion) is degenerated with that with $N_{\rm sk} = -1$ (skyrmion) owing to the absence of the bond-dependent anisotropy [69]; it is noted that the helicity of skyrmion is not fixed, which is also attributed to the absence of the bond-dependent anisotropy. The structure factor exhibits the fourfold-symmetric peak structures as follows: $J_{\boldsymbol{Q}_1}^{xy} = J_{\boldsymbol{Q}_2}^{xy}$, $J_{\boldsymbol{Q}_1}^z = J_{\boldsymbol{Q}_2}^z$, $J_{\boldsymbol{Q}_1'}^{xy} = J_{\boldsymbol{Q}_2'}^{xy}$, and $J_{\boldsymbol{Q}_1'}^z = J_{\boldsymbol{Q}_2'}^z$ as shown in Fig. 2(b) and Fig. 3.

The magnetic-moment configuration of the S-SkL is approximately expressed as

$$\boldsymbol{J}_i \propto \begin{pmatrix} -\cos\mathcal{Q}_1 + \cos\mathcal{Q}_2 \\ -\cos\mathcal{Q}_1 - \cos\mathcal{Q}_2 \\ -a_z(\sin\mathcal{Q}_1 + \sin\mathcal{Q}_2) + \tilde{h}_z \end{pmatrix}^{\mathrm{T}},$$ (25)

where $\mathcal{Q}_\eta = \boldsymbol{Q}_\eta \cdot \boldsymbol{r}_i + \theta_\eta$ for $\eta = 1, 2$. The a_z and $\tilde{h}_z$ stand for the parameters related to the degree of the easy-axis magnetic anisotropy and uniform magnetization, respectively. By empirically choosing the parameters to approximately reproduce the real-space magnetic-moment configuration of the S-SkL obtained by the mean-field calculations in Fig. 2(a), we obtain $a_z \simeq 4$, $\tilde{h}_z \simeq 3.5$, $\theta_1 \in (0, \frac{\pi}{4})$ [or $(-\frac{\pi}{4}, 0)$], and $\theta_2 \in (-\frac{\pi}{4}, 0)$ [or $(0, \frac{\pi}{4})$], normalizing the magnetic moments and scaling them by the length $l \simeq 2.4$. The relatively large value of a_z indicates that the energy gain from the easy-axis magnetic anisotropy plays an important role in stabilizing the S-SkL. Indeed, the magnetic moments consisting of the S-SkL are distributed in the vicinity of the north and south poles in the unit sphere, as shown in Fig. 4. The top view in Fig. 4(b) demonstrates the fourfold rotational symmetry of the S-SkL.
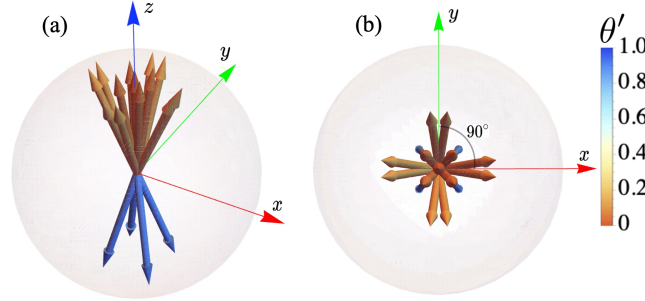

FIG. 4. A schematic of real-space magnetic moments plotted on the surface of a unit sphere, where the magnetic moments forming the S-SkL are distributed primarily near the north and south poles. (a): Default view. (b): Top view.

In addition to the S-SkL, we find another double-Q state with a net scalar chirality, which is denoted as the $2Q$ II state in the phase diagram in Fig. 1. This state is stabilized in the narrow regions of Δ and h: $0.5 \lesssim \Delta \lesssim 0.64$ and $0 \leq h \lesssim 0.15$. Similar to the S-SkL, this state accompanies a net scalar chirality, as shown in the bottom panel of Fig. 3(b). On the other hand, the skyrmion number of this phase fluctuates depending on Δ; the skyrmion number is zero for $0.5 \lesssim \Delta \lesssim 0.6$, whereas it is one for $0.6 \lesssim \Delta \lesssim 0.64$. The reason why the different skyrmion numbers might be attributed to the almost coplanar magnetic-moment configuration in the $2Q$ II state. As shown in the real-space magnetic-moment distribution in Figs. 5(a) and 5(b), almost all of the magnetic moments are distributed in the same plane, although there is a slightly out-of-plane component. This indicates the finite scalar chirality with the large solid angle owing to the strong easy-axis anisotropy, which leads to the sign change sensitive to the moment direction. In addition, the magnetic-moment configuration of this state breaks the fourfold rotational symmetry, as clearly found in Fig. 5(b). It is noted that this state also emerges thanks to the multi-orbital effect, which has not been reported in the classical spin model, where only the zero-field SkL phase with the skyrmion number of two has been found in centrosymmetric hosts [50, 70].
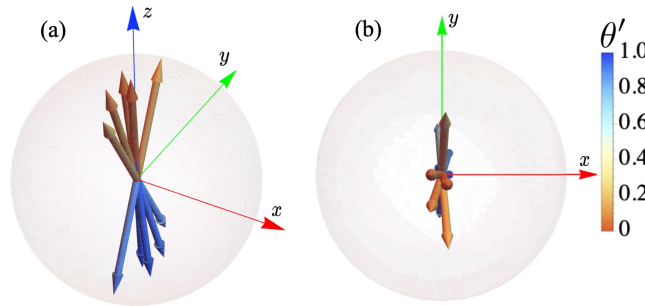

FIG. 5. A schematic of real-space magnetic moments plotted on the surface of a unit sphere, illustrating the $2Q$ II state. The magnetic moments near the north and south poles of the unit sphere are nearly collinear. (a): Default view. (b): Top view.

Finally, let us briefly discuss the characteristics of the other magnetic phases in the phase diagram. Except for the S-SkL and the $2Q$ II state, we identify one single-Q state and five types of other double-Q states. We summarize the nonzero components of $J_{\boldsymbol{Q}_\eta}$ and $J_{\boldsymbol{Q}'_\eta}$ in Table I. The $1Q$ conical state with the intensity at $\boldsymbol{Q}_1$ or $\boldsymbol{Q}_2$ is stabilized across all Δ in the high-field region; the spiral plane lies in the xy plane. The critical value of the magnetic field to this state is approximately $h \simeq 1.3$. This state turns into the ferromagnetic state, where the critical magnetic field varies linearly with Δ, as shown in Fig. 1. The $2Q$ I state is stabilized at $0 \leq \Delta < 0.5$ and in the small magnetic field around $0 \leq h < 0.2$, occupying a narrow region of the phase diagram. The $2Q$ I state is the only double-Q state that lacks local scalar chirality χ_i, as shown in Fig. 2(c). In other words, this state is characterized by the coplanar magnetic-moment configuration, as shown by the real-space configuration in Fig. 2(a). As the crystal field splitting Δ increases, the $2Q$ I state within $h < 0.2$ undergoes continuous deformation through the $2Q$ II state with a net scalar chirality, and eventually transform into the $2Q$ III state. The $2Q$ III state is stabilized for $\Delta > 0.64$. The in-plane and out-of-plane components of the structure factor in the $2Q$ III state closely resemble those of the $2Q$ I and $2Q$ II states, as shown in Fig. 2(b) and Fig. 3, although the relation of $J_{\boldsymbol{Q}'_1}^z = J_{\boldsymbol{Q}'_2}^z$ in the $2Q$ I and $2Q$ II states no longer holds. When Δ increases, the values of $J_{\boldsymbol{Q}'_1}^z$, $J_{\boldsymbol{Q}'_2}^{xy}$, and $J_{\boldsymbol{Q}_2}^{xy}$ rapidly decrease , as shown in the top panel of Fig. 3(c). The $2Q$ IV state is stabilized for all Δ up to $\Delta = 4$, emerging at $h > 0.15$. In the region $0 \leq \Delta \lesssim 1$, the critical magnetic field separating the $2Q$ IV and $2Q$ V states increases linearly until $h \simeq 0.95$. Beyond this point, the $2Q$ V state disappears, and the upper bound of the $2Q$ IV state remains at $h \simeq 1.0$, as shown in Fig. 1. The lack of fourfold rotational symmetry in the $2Q$ IV state is due to $J_{\boldsymbol{Q}_1} \neq J_{\boldsymbol{Q}_2}$, as demonstrated in Fig. 2(b) and Fig. 3. The $2Q$ V state is stabilized at $0 \leq \Delta \lesssim 1$. As Δ increases, the region occupied by the $2Q$ V state shrinks. Although this state satisfies $J_{\boldsymbol{Q}_1} = J_{\boldsymbol{Q}_2}$, inhomogeneous contributions from higher-harmonic wave vectors break the fourfold rotational symmetry, as seen in Fig. 2(b) and Fig. 3(a)–(b). The $2Q$ VI state emerges for $3.2 < \Delta$ within the magnetic field ranged around $0.9 \lesssim h \lesssim 1.15$. This state replaces the S-SkL region in the phase diagram. As shown in Fig. 2(b) and Fig. 3(c), high-harmonic wave vectors contribute to the fourfold rotational symmetry, as indicated by the relations $J_{\boldsymbol{Q}'_1}^z = J_{\boldsymbol{Q}'_2}^z$. However, the inequality $J_{\boldsymbol{Q}_1}^{xy} \neq J_{\boldsymbol{Q}_2}^{xy}$ signifies the breaking of this symmetry. In this way, the competing interactions in multi-orbital systems give rise to a rich variety of multi-Q states as the lowest-energy configurations.

V. SUMMARY

To summarize, we have investigated the emergence of the S-SkL on a centrosymmetric square lattice by employing mean-field calculations with an emphasis on the multi-orbital degree of freedom. By taking into account the effects of the atomic spin–orbit coupling and tetragonal crystalline electric field, we have constructed an effective localized model consisting of two Kramers doublets with easy-axis magnetic anisotropy. Then, we have clarified the low-temperature phase diagram, which includes the S-SkL with the skyrmion number of one and the double-Q state with the nonzero scalar chirality ($2Q$ II). We have shown that the multi-orbital effect assists the stabilization of the S-SkL and the $2Q$ II state by changing the crystal-field splitting between two Kramers doublets. We also found that a variety of double-Q states can be realized in the multi-orbital model. Our study reveals a possibility of stabilizing S-SkLs in $4f$-electron systems with a finite orbital angular momentum $\boldsymbol{L} \neq \boldsymbol{0}$, as found in the Ce^{3+} ion on a centrosymmetric square lattice. This finding opens a new avenue for subsequent studies on skyrmion-hosting materials with the orbital degree of freedom.

ACKNOWLEDGMENTS

Appendix A: Derivation of the atomic bases

In this Appendix, we show the derivation of the atomic bases in Eq. (1) in the main text. In a $4f$-electron wave function with the f^1 configuration to have the orbital angular momentum $L = 3$ in the presence of the spherical symmetry, there are $(2J + 1)$-fold degenerate states. Such a degeneracy is lifted when the relativistic spin–orbit coupling and the crystalline electric field are considered. First, we consider the effect of the spin–orbit coupling,

whose Hamiltonian is given by

$$\mathcal{H}_{LS} = \lambda \, \boldsymbol{L} \cdot \boldsymbol{S}, \tag{A1}$$

where $\boldsymbol{L} = (L^x, L^y, L^z)$ and $\boldsymbol{S} = (S^x, S^y, S^z)$ stand for the orbital and spin angular momentum operators, respectively. λ represents the spin–orbit coupling constant. This leads to the energy splittings into the eightfold-degenerated multiplet with $J = \frac{7}{2}$ and sixfold-degenerated multiplet with $J = \frac{5}{2}$. Hereafter, we focus on the $J = \frac{5}{2}$ multiplet by supposing the larger spin–orbit coupling.

Next, we take into account the effect of the tetragonal crystalline electric field, which further splits the above-degenerated bands into three Kramers doublets. The crystal field Hamiltonian is given by

$$\mathcal{H}_{\mathrm{cry}} = B_2^0 O_2^0 + B_4^0 O_4^0 + B_4^4 O_4^4, \tag{A2}$$

where B_2^0, B_4^0, and B_4^4 are the crystal field parameters. The Stevens operator, O_n^m, is defined by [71, 72]

$$
\begin{aligned}
O_2^0 &= 3J_z^2 - \boldsymbol{J}^2, \\
O_4^0 &= 35J_z^4 - 30\boldsymbol{J}^2 J_z^2 + 25J_z^2 - 6\boldsymbol{J}^2 + 3\boldsymbol{J}^4, \\
O_4^4 &= \frac{1}{2}\left[(J^+)^4 + (J^-)^4\right].
\end{aligned} \tag{A3}
$$

By applying $\mathcal{H}_{\mathrm{cry}}$ to the sixfold $J = \frac{5}{2}$ basis, the matrix element of the crystal field Hamiltonian is expressed as

$$
\begin{pmatrix}
10(B_2^0 + 6B_4^0) & 0 & 0 & 0 & 12\sqrt{5}B_4^4 & 0 \\
0 & -2(B_2^0 + 90B_4^0) & 0 & 0 & 0 & 12\sqrt{5}B_4^4 \\
0 & 0 & -8(B_2^0 - 15B_4^0) & 0 & 0 & 0 \\
0 & 0 & 0 & -8(B_2^0 - 15B_4^0) & 0 & 0 \\
12\sqrt{5}B_4^4 & 0 & 0 & 0 & -2(B_2^0 + 90B_4^0) & 0 \\
0 & 12\sqrt{5}B_4^4 & 0 & 0 & 0 & 10(B_2^0 + 6B_4^0)
\end{pmatrix}, \tag{A4}
$$

where the order of the basis wave function is represented by $|5/2, J^z\rangle$, from $|5/2, 5/2\rangle$ down to $|5/2, -5/2\rangle$. The eigenvalues are given by

$$
\begin{aligned}
&- 8(B_2^0 - 15B_4^0), \\
&- 6\sqrt{(B_2^0 + 20B_4^0)^2 + 20(B_4^4)^2} + 4B_2^0 - 60B_4^0, \\
&6\sqrt{(B_2^0 + 20B_4^0)^2 + 20(B_4^4)^2} + 4B_2^0 - 60B_4^0,
\end{aligned}
$$

where the corresponding eigenstates are given by

$$
\begin{cases}
\left|\Gamma_{t6\pm}\right\rangle = \left|\frac{5}{2}, \pm\frac{1}{2}\right\rangle, \\
\left|\Gamma_{t7\pm}^{(1)}\right\rangle = \alpha\left|\frac{5}{2}, \pm\frac{5}{2}\right\rangle - \beta\left|\frac{5}{2}, \mp\frac{3}{2}\right\rangle, \\
\left|\Gamma_{t7\pm}^{(2)}\right\rangle = \beta\left|\frac{5}{2}, \pm\frac{5}{2}\right\rangle + \alpha\left|\frac{5}{2}, \mp\frac{3}{2}\right\rangle,
\end{cases} \tag{A5}
$$

respectively. Here, α and β are given in the main text.

In the localized model, we appropriately choose the crystal field parameters so that two bases $\left|\Gamma_{t7\pm}^{(1)}\right\rangle$ and $\left|\Gamma_{t7\pm}^{(2)}\right\rangle$ are relevant in the targeting physical space for simplicity. We then set the atomic energy levels of $\left|\Gamma_{t7\pm}^{(1)}\right\rangle$ and $\left|\Gamma_{t7\pm}^{(2)}\right\rangle$ to 0 and Δ, respectively.

Appendix B: Other superposition coefficients α

In this Appendix, we discuss the stability of S-SkL for different choices of α in Eq. (1) at $\Delta = 2$. Figure 6 provides an overview of the phase diagrams for $\alpha = 0.3, 0.38, 0.408, 0.6124,$ and 0.65; the result at $\alpha = 0.38$ is the same as that in Fig. 1. In all the cases, the S-SkL phase appears in the phase diagram. Especially, it is noteworthy that the S-SkL
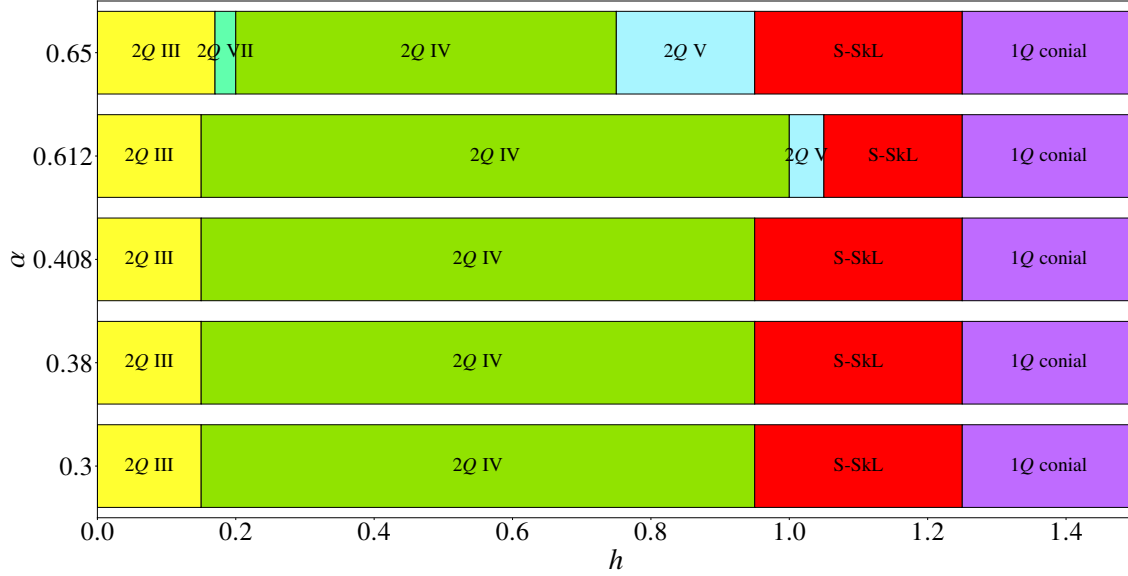
FIG. 6. Phase diagrams for several representative values of α under $\Delta = 2$. Each panel corresponds to a different value of α: 0.3, 0.38, 0.408, 0.612, and 0.65 (from bottom to top). The vertical axis denotes α, while the horizontal axis denotes the external magnetic field h, ranging from 0 to 1.5.

survives even when the xy-plane components in $\boldsymbol{J}$ are larger than the z-axis for $\alpha = 0.6124$ and 0.65. We find that the essence to stabilize the S-SkL for $\alpha = 0.6124$ and 0.65 is the off-diagonal component of $\boldsymbol{J}$ between the $\left|\Gamma_{t7\pm}^{(1)}\right\rangle$ and $\left|\Gamma_{t7\pm}^{(2)}\right\rangle$ levels, which favors the easy-axis-type magnetic-moment configuraiton.

We also obtain an additional phase (2Q VII) for $\alpha = 0.65$, which appears in the narrow field region around $0.17 \lesssim h \lesssim 0.2$. This phase is characterized by a nonzero net magnetization $|\langle \boldsymbol{J} \rangle| \simeq 0.21$ as well as the double-Q modulations at $\boldsymbol{Q}_1$ and $\boldsymbol{Q}_2$, which varies with the applied magnetic field. We list the nonzero components of $J_{\boldsymbol{Q}_\eta}$ and $J_{\boldsymbol{Q}'_\eta}$ ($\eta = 1, 2$) in the 2Q VII phase in Table II.

TABLE II. Nonzero components of $J_{\boldsymbol{Q}_\eta}$ and $J_{\boldsymbol{Q}'_\eta}$ ($\eta = 1, 2$) in phase 2Q VII.

phase	$J_{\boldsymbol{Q}_1}$, $J_{\boldsymbol{Q}_2}$ ($\boldsymbol{Q}_\eta \parallel [110]$)	$J_{\boldsymbol{Q}'_1}$, $J_{\boldsymbol{Q}'_2}$ ($\boldsymbol{Q}'_\eta \parallel [100]$)
2Q VII	$J_{\boldsymbol{Q}_1}^{xy} = J_{\boldsymbol{Q}_2}^{xy}$, $J_{\boldsymbol{Q}_1}^{z} = J_{\boldsymbol{Q}_2}^{z}$	$J_{\boldsymbol{Q}'_1}^{xy}$, $J_{\boldsymbol{Q}'_1}^{z}$, $J_{\boldsymbol{Q}'_2}^{z}$

[1] T. Skyrme, A unified field theory of mesons and baryons, Nuclear Physics **31**, 556 (1962).
[2] A. Bogdanov and D. Yablonskiui, Thermodynamically stable "vortices" in magnetically ordered crystals. the mixed state of magnets, Sov. Phys. JETP **68**, 101 (1989).
[3] A. Bogdanov and A. Hubert, Thermodynamically stable magnetic vortex states in magnetic crystals, Journal of Magnetism and Magnetic Materials **138**, 255 (1994).
[4] U. K. Roessler, A. Bogdanov, and C. Pfleiderer, Spontaneous skyrmion ground states in magnetic metals, Nature **442**, 797 (2006).
[5] N. Nagaosa and Y. Tokura, Topological properties and dynamics of magnetic skyrmions, Nature nanotechnology **8**, 899 (2013).
[6] X. Zhang, Y. Zhou, K. M. Song, T.-E. Park, J. Xia, M. Ezawa, X. Liu, W. Zhao, G. Zhao, and S. Woo, Skyrmion-electronics: writing, deleting, reading and processing magnetic skyrmions toward spintronic applications, Journal of Physics: Condensed Matter **32**, 143001 (2020).

[7] B. Göbel, I. Mertig, and O. A. Tretiakov, Beyond skyrmions: Review and perspectives of alternative magnetic quasiparticles, Physics Reports **895**, 1 (2021).

[8] S. Hayami and Y. Motome, Topological spin crystals by itinerant frustration, Journal of Physics: Condensed Matter **33**, 443001 (2021).

[9] X. Zhang, Y. Zhou, and M. Ezawa, Antiferromagnetic skyrmion: stability, creation and manipulation, Scientific reports **6**, 24795 (2016).

[10] H. Oike, A. Kikkawa, N. Kanazawa, Y. Taguchi, M. Kawasaki, Y. Tokura, and F. Kagawa, Interplay between topological and thermodynamic stability in a metastable magnetic skyrmion lattice, Nature Physics **12**, 62 (2016).

[11] D. Cortés-Ortuño, W. Wang, M. Beg, R. A. Pepper, M.-A. Bisotti, R. Carey, M. Vousden, T. Kluyver, O. Hovorka, and H. Fangohr, Thermal stability and topological protection of skyrmions in nanotracks, Scientific reports **7**, 4060 (2017).

[12] S.-G. Je, H.-S. Han, S. K. Kim, S. A. Montoya, W. Chao, I.-S. Hong, E. E. Fullerton, K.-S. Lee, K.-J. Lee, M.-Y. Im, *et al.*, Direct demonstration of topological stability of magnetic skyrmions via topology manipulation, ACS nano **14**, 3251 (2020).

[13] A. Fert, V. Cros, and J. Sampaio, Skyrmions on the track, Nature nanotechnology **8**, 152 (2013).

[14] N. Romming, C. Hanneken, M. Menzel, J. E. Bickel, B. Wolter, K. von Bergmann, A. Kubetzka, and R. Wiesendanger, Writing and deleting single magnetic skyrmions, Science **341**, 636 (2013).

[15] A. Fert, N. Reyren, and V. Cros, Magnetic skyrmions: advances in physics and potential applications, Nature Reviews Materials **2**, 1 (2017).

[16] I. Dzyaloshinsky, A thermodynamic theory of "weak" ferromagnetism of antiferromagnetics, Journal of Physics and Chemistry of Solids **4**, 241 (1958).

[17] T. Moriya, Anisotropic superexchange interaction and weak ferromagnetism, Phys. Rev. **120**, 91 (1960).

[18] S. D. Yi, S. Onoda, N. Nagaosa, and J. H. Han, Skyrmions and anomalous hall effect in a dzyaloshinskii-moriya spiral magnet, Phys. Rev. B **80**, 054416 (2009).

[19] T. Kurumaji, T. Nakajima, M. Hirschberger, A. Kikkawa, Y. Yamasaki, H. Sagayama, H. Nakao, Y. Taguchi, T.-h. Arima, and Y. Tokura, Skyrmion lattice with a giant topological hall effect in a frustrated triangular-lattice magnet, Science **365**, 914 (2019).

[20] M. Hirschberger, L. Spitz, T. Nomoto, T. Kurumaji, S. Gao, J. Masell, T. Nakajima, A. Kikkawa, Y. Yamasaki, H. Sagayama, H. Nakao, Y. Taguchi, R. Arita, T.-h. Arima, and Y. Tokura, Topological nernst effect of the two-dimensional skyrmion lattice, Phys. Rev. Lett. **125**, 076602 (2020).

[21] M. Hirschberger, T. Nakajima, M. Kriener, T. Kurumaji, L. Spitz, S. Gao, A. Kikkawa, Y. Yamasaki, H. Sagayama, H. Nakao, S. Ohira-Kawamura, Y. Taguchi, T.-h. Arima, and Y. Tokura, High-field depinned phase and planar hall effect in the skyrmion host gd_2pdsi_3, Phys. Rev. B **101**, 220401 (2020).

[22] S. Spachmann, A. Elghandour, M. Frontzek, W. Löser, and R. Klingeler, Magnetoelastic coupling and phases in the skyrmion lattice magnet gd_2pdsi_3 discovered by high-resolution dilatometry, Phys. Rev. B **103**, 184424 (2021).

[23] J. A. M. Paddison, B. K. Rai, A. F. May, S. Calder, M. B. Stone, M. D. Frontzek, and A. D. Christianson, Magnetic interactions of the centrosymmetric skyrmion material Gd_2PdSi_3, Phys. Rev. Lett. **129**, 137202 (2022).

[24] M. Hirschberger, T. Nakajima, S. Gao, L. Peng, A. Kikkawa, T. Kurumaji, M. Kriener, Y. Yamasaki, H. Sagayama, H. Nakao, *et al.*, Skyrmion phase and competing magnetic orders on a breathing kagomé lattice, Nature communications **10**, 5831 (2019).

[25] M. Hirschberger, S. Hayami, and Y. Tokura, Nanometric skyrmion lattice from anisotropic exchange interactions in a centrosymmetric host, New J. Phys. **23**, 023039 (2021).

[26] S. Nakamura, N. Kabeya, M. Kobayashi, K. Araki, K. Katoh, and A. Ochiai, Magnetic phases of the frustrated ferromagnetic spin-trimer system $Gd_3Ru_4Al_{12}$ with a distorted kagome lattice structure, Phys. Rev. B **107**, 014422 (2023).

[27] N. D. Khanh, T. Nakajima, X. Yu, S. Gao, K. Shibata, M. Hirschberger, Y. Yamasaki, H. Sagayama, H. Nakao, L. Peng, *et al.*, Nanometric square skyrmion lattice in a centrosymmetric tetragonal magnet, Nature Nanotechnology **15**, 444 (2020).

[28] N. D. Khanh, T. Nakajima, S. Hayami, S. Gao, Y. Yamasaki, H. Sagayama, H. Nakao, R. Takagi, Y. Motome, Y. Tokura, *et al.*, Zoology of multiple-q spin textures in a centrosymmetric tetragonal magnet with itinerant electrons, Advanced Science **9**, 2105452 (2022).

[29] G. D. A. Wood, D. D. Khalyavin, D. A. Mayoh, J. Bouaziz, A. E. Hall, S. J. R. Holt, F. Orlandi, P. Manuel, S. Blügel, J. B. Staunton, O. A. Petrenko, M. R. Lees, and G. Balakrishnan, Double-q ground state with topological charge stripes in the centrosymmetric skyrmion candidate $GdRu_2Si_2$, Phys. Rev. B **107**, L180402 (2023).

[30] T. Shang, Y. Xu, D. J. Gawryluk, J. Z. Ma, T. Shiroka, M. Shi, and E. Pomjakushina, Anomalous hall resistivity and possible topological hall effect in the $eual_4$ antiferromagnet, Phys. Rev. B **103**, L020405 (2021).

[31] K. Kaneko, T. Kawasaki, A. Nakamura, K. Munakata, A. Nakao, T. Hanashima, R. Kiyanagi, T. Ohhara, M. Hedo, T. Nakama, and Y. Ōnuki, Charge-density-wave order and multiple magnetic transitions in divalent europium compound eual4, Journal of the Physical Society of Japan **90**, 064704 (2021), https://doi.org/10.7566/JPSJ.90.064704.

[32] R. Takagi, N. Matsuyama, V. Ukleev, L. Yu, J. S. White, S. Francoual, J. R. Mardegan, S. Hayami, H. Saito, K. Kaneko, *et al.*, Square and rhombic lattices of magnetic skyrmions in a centrosymmetric binary compound, Nature communications **13**, 1472 (2022).

[33] W. R. Meier, J. R. Torres, R. P. Hermann, J. Zhao, B. Lavina, B. C. Sales, and A. F. May, Thermodynamic insights into the intricate magnetic phase diagram of eual$_4$, Phys. Rev. B **106**, 094421 (2022).

[34] M. Gen, R. Takagi, Y. Watanabe, S. Kitou, H. Sagayama, N. Matsuyama, Y. Kohama, A. Ikeda, Y. Ōnuki, T. Kurumaji, T.-h. Arima, and S. Seki, Rhombic skyrmion lattice coupled with orthorhombic structural distortion in eual$_4$, Phys. Rev. B **107**, L020410 (2023).

[35] H. Yoshimochi, R. Takagi, J. Ju, N. Khanh, H. Saito, H. Sagayama, H. Nakao, S. Itoh, Y. Tokura, T. Arima, *et al.*, Multistep topological transitions among meron and skyrmion crystals in a centrosymmetric magnet, Nature Physics **20**, 1001 (2024).

[36] S. Hayami and R. Yambe, Stabilization mechanisms of magnetic skyrmion crystal and multiple-q states based on momentum-resolved spin interactions, Mater. Today Quantum **3**, 100010 (2024).

[37] T. Okubo, S. Chung, and H. Kawamura, Multiple-q states and the skyrmion lattice of the triangular-lattice heisenberg antiferromagnet under magnetic fields, Phys. Rev. Lett. **108**, 017206 (2012).

[38] A. O. Leonov and M. Mostovoy, Multiply periodic states and isolated skyrmions in an anisotropic frustrated magnet, Nat. Commun. **6**, 8275 (2015).

[39] S.-Z. Lin and S. Hayami, Ginzburg-Landau theory for skyrmions in inversion-symmetric magnets with competing interactions, Phys. Rev. B **93**, 064430 (2016).

[40] O. I. Utesov, Thermodynamically stable skyrmion lattice in a tetragonal frustrated antiferromagnet with dipolar interaction, Phys. Rev. B **103**, 064414 (2021).

[41] O. I. Utesov, Mean-field description of skyrmion lattice in hexagonal frustrated antiferromagnets, Phys. Rev. B **105**, 054435 (2022).

[42] S. Hayami, S.-Z. Lin, Y. Kamiya, and C. D. Batista, Vortices, skyrmions, and chirality waves in frustrated Mott insulators with a quenched periodic array of impurities, Phys. Rev. B **94**, 174420 (2016).

[43] D. Amoroso, P. Barone, and S. Picozzi, Spontaneous skyrmionic lattice from anisotropic symmetric exchange in a Ni-halide monolayer, Nat. Commun. **11**, 5784 (2020).

[44] S. Hayami and Y. Motome, Noncoplanar multiple-Q spin textures by itinerant frustration: Effects of single-ion anisotropy and bond-dependent anisotropy, Phys. Rev. B **103**, 054422 (2021).

[45] R. Yambe and S. Hayami, Effective spin model in momentum space: Toward a systematic understanding of multiple-Q instability by momentum-resolved anisotropic exchange interactions, Phys. Rev. B **106**, 174437 (2022).

[46] H. Zhang and S.-Z. Lin, Multipolar Skyrmion Crystals in Non-Kramers Doublet Systems, Phys. Rev. Lett. **133**, 196702 (2024).

[47] R. Yambe and S. Hayami, Dynamical generation of skyrmion and bimeron crystals by a circularly polarized electric field in frustrated magnets, Physical Review B **110**, 014428 (2024).

[48] S. Hayami, S.-Z. Lin, and C. D. Batista, Bubble and skyrmion crystals in frustrated magnets with easy-axis anisotropy, Phys. Rev. B **93**, 184413 (2016).

[49] S. Hayami and Y. Motome, Square skyrmion crystal in centrosymmetric itinerant magnets, Phys. Rev. B **103**, 024439 (2021).

[50] Z. Wang, Y. Su, S.-Z. Lin, and C. D. Batista, Meron, skyrmion, and vortex crystals in centrosymmetric tetragonal magnets, Phys. Rev. B **103**, 104408 (2021).

[51] S. Hayami, Rectangular and square skyrmion crystals on a centrosymmetric square lattice with easy-axis anisotropy, Phys. Rev. B **105**, 174437 (2022).

[52] K. Okigami and S. Hayami, Exploring topological spin order by inverse Hamiltonian design: A stabilization mechanism for square skyrmion crystals, Phys. Rev. B **110**, L220405 (2024).

[53] X. Y. Zhu, H. Zhang, D. J. Gawryluk, Z. X. Zhen, B. C. Yu, S. L. Ju, W. Xie, D. M. Jiang, W. J. Cheng, Y. Xu, M. Shi, E. Pomjakushina, Q. F. Zhan, T. Shiroka, and T. Shang, Spin order and fluctuations in the EuAl$_4$ and EuGa$_4$ topological antiferromagnets: A μSR study, Phys. Rev. B **105**, 014423 (2022).

[54] H. Zhang, X. Zhu, Y. Xu, D. Gawryluk, W. Xie, S. Ju, M. Shi, T. Shiroka, Q. Zhan, E. Pomjakushina, and T. Shang, Giant magnetoresistance and topological Hall effect in the euga$_4$ antiferromagnet, J. Phys.: Condens. Matter **34**, 034005 (2022).

[55] J. M. Moya, S. Lei, E. M. Clements, C. S. Kengle, S. Sun, K. Allen, Q. Li, Y. Y. Peng, A. A. Husain, M. Mitrano, M. J. Krogstad, R. Osborn, A. B. Puthirath, S. Chi, L. Debeer-Schmitt, J. Gaudet, P. Abbamonte, J. W. Lynn, and E. Morosan, Incommensurate magnetic orders and topological Hall effect in the square-net centrosymmetric euga$_2$al$_2$ system, Phys. Rev. Materials **6**, 074201 (2022).

[56] M. R. U. Nabi, A. Wegner, F. Wang, Y. Zhu, Y. Guan, A. Fereidouni, K. Pandey, R. Basnet, G. Acharya, H. O. H. Churchill, Z. Mao, and J. Hu, Giant topological Hall effect in centrosymmetric tetragonal mn$_{2-x}$zn$_x$Sb, Phys. Rev. B **104**, 174419 (2021).

[57] H. Hayashi, M. Kato, T. Terashima, N. Kikugawa, H. Sakurai, H. K. Yoshida, and K. Yamaura, Exploring the Magnetic Phase Diagram and Hall Resistivity Suppression in Centrosymmetric GdOs$_2$Si$_2$ Single Crystal, J. Phys. Soc. Jpn. **93**, 094702 (2024).

[58] M. Sundermann, A. Amorese, F. Strigari, B. Leedahl, L. H. Tjeng, M. W. Haverkort, H. Gretarsson, H. Yavaş, M. M. Sala, E. D. Bauer, P. F. S. Rosa, J. D. Thompson, and A. Severing, Orientation of the ground-state orbital in CeCoIn$_5$ and CeRhIn$_5$, Phys. Rev. B **99**, 235143 (2019).

[59] N. Iwahara and L. F. Chibotaru, Exchange interaction between j multiplets, Phys. Rev. B **91**, 174438 (2015).

[60] A. Yoshimori, A new type of antiferromagnetic structure in the rutile type crystal, Journal of the Physical Society of Japan **14**, 807 (1959), https://doi.org/10.1143/JPSJ.14.807.

[61] S. Hayami and Y. Motome, Effect of magnetic anisotropy on skyrmions with a high topological number in itinerant magnets, Phys. Rev. B **99**, 094420 (2019).

[62] P. Weiss, L'hypothèse du champ moléculaire et la propriété ferromagnétique, J. Phys. Theor. Appl. **6**, 661 (1907).

[63] A. Weiße and H. Fehske, Exact diagonalization techniques, in *Computational Many-Particle Physics*, edited by H. Fehske, R. Schneider, and A. Weiße (Springer Berlin Heidelberg, Berlin, Heidelberg, 2008) pp. 529–544.

[64] X. G. Wen, F. Wilczek, and A. Zee, Chiral spin states and superconductivity, Phys. Rev. B **39**, 11413 (1989).

[65] R. Rajaraman, *Solitons and Instantons. An Introduction to Solitons and Instantons in Quantum Field Theory* (Elsevier, 1987).

[66] H.-B. Braun, Topological effects in nanomagnetism: from superparamagnetism to chiral quantum solitons, Advances in Physics **61**, 1 (2012).

[67] B. Berg and M. Lüscher, Definition and statistical distributions of a topological number in the lattice o (3) σ-model, Nuclear Physics B **190**, 412 (1981).

[68] At $\Delta = 0$, the magnetic moment length $|\langle \boldsymbol{J}_i \rangle|$ varies from 2.47 ($2Q$ I) to 2.50 (Ferro) as the magnetic field increases. At $\Delta = 4$, $|\langle \boldsymbol{J}_i \rangle|$ varies from 2.27 ($2Q$ III) to 2.49 (Ferro) as the magnetic field increases.

[69] S. Hayami and R. Yambe, Degeneracy lifting of Néel, Bloch, and anti-skyrmion crystals in centrosymmetric tetragonal systems, J. Phys. Soc. Jpn. **89**, 103702 (2020).

[70] S. Hayami, Multiple skyrmion crystal phases by itinerant frustration in centrosymmetric tetragonal magnets, J. Phys. Soc. Jpn. **91**, 023705 (2022).

[71] K. Stevens, Matrix elements and operator equivalents connected with the magnetic properties of rare earth ions, Proceedings of the Physical Society. Section A **65**, 209 (1952).

[72] M. T. Hutchings, Point-charge calculations of energy levels of magnetic ions in crystalline electric fields, in *Solid state physics*, Vol. 16 (Elsevier, 1964) pp. 227–273.